International Journal of Nanomedicine

Dovepress
open access to scientific and medical research

Open Access Full Text Article

ORIGINAL RESEARCH

One-Step Preparation of an AgNP-nHA@RGO Three-Dimensional Porous Scaffold and Its Application in Infected Bone Defect Treatment

This article was published in the following Dove Press journal:
International Journal of Nanomedicine

Weizong Weng[1,2,*]
Xiaoqun Li[1,*]
Wei Nie[3]
Haoyuan Liu[2]
Shanshan Liu[2]
Jianming Huang[2]
Qirong Zhou[1]
Jia He[1]
Jiacan Su[1]
Zhifeng Dong[4]
Dongliang Wang[5]

[1]Department of Orthopeadics, Changhai Hospital affiliated to the Second Military Medical University, Shanghai 200433, People's Republic of China; [2]Orthopaedics Department, Chenggong Hospital Affilaited to Xiamen University, Xiamen 361000, People's Republic of China; [3]College of Chemistry, Chemical Engineering and Biotechnology, State Key Laboratory for Modification of Chemical Fibers and Polymer Materials, Donghua University, Shanghai 201620, People's Republic of China; [4]Department of Cardiology, Shanghai Sixth Hospital, Shanghai Jiaotong University, School of Medicine, Shanghai 200233, People's Republic of China; [5]Orthopeadics Department, Xinhua Hospital Affiliated to the Shanghai Jiaotong University, Shanghai 200433, People's Republic of China

*These authors contributed equally to this work

Correspondence: Dongliang Wang; Weizong Weng
Email wangdongliang@xinhuanmed.com.cn; drwengweizong@163.com

Background: Bactericidal capacity, durable inhibition of biofilm formation, and a three-dimensional (3D) porous structure are the emphases of infected bone defect (IBD) treatment via local scaffold implantation strategy.

Purpose: In this study, silver nanoparticle (AgNP)-loaded nano-hydroxyapatite (nHA)@ reduced graphene oxide (RGO) 3D scaffolds (AHRG scaffolds) were designed to alleviate bone infection, inhibit biofilm formation, and promote bone repair through the synergistic effects of AgNPs, RGO, and nHA.

Materials and Methods: AHRGs were prepared using a one-step preparation method, to create a 3D porous scaffold to facilitate a uniform distribution of AgNPs and nHA. Methicillin-resistant Staphylococcus aureus (MRSA) was used as a model-resistant bacterium, and the effects of different silver loadings on the antimicrobial activity and cytocompatibility of materials were evaluated. Finally, a rabbit IBD model was used to evaluate the therapeutic effect of the AHRG scaffold in vivo.

Results: The results showed successful synthesis of the AHRG scaffold. The ideal 3D porous structure was verified using scanning electron microscopy and transmission electron microscopy, and X-ray photoelectron spectroscopy and selected area electron diffraction measurements revealed uniform distributions of AgNP and nHA. In vitro antibacterial and cytocompatibility indicated that the 4% AHRG scaffolds possessed the most favorable balance of bactericidal properties and cytocompatibility. In vivo evaluation of the IBD model showed promising treatment efficacy of AHRG scaffolds.

Conclusion: The as-fabricated AHRG scaffolds effectively eliminated infection and inhibited biofilm formation. IBD repair was facilitated by the bactericidal properties and 3D porous structure of the AHRG scaffold, suggesting its potential in the treatment of IBDs.

Keywords: biofilm, graphene oxide, hydroxyapatite, infected bone defect, scaffold, silver nanoparticles, three-dimensional

Introduction

Clinical treatment of infected bone defects (IBDs) has always been a challenge, due to persistent bacterium colonization and osteonecrosis.[1,2] Conventional disinfection approaches, such as debridement and systemic antibiotics, may lead to secondary trauma or toxic effects.[1,3] To overcome these drawbacks, antibiotic-impregnated porous scaffolds have been introduced as an IBD treatment in recent years.[1,3–5] The treatment of IBD with these scaffolds significantly increases the local antibiotic concentration, thus providing protection against infection.[5–7] Moreover, the porous

architecture of the scaffold can facilitate bone tissue regeneration,[8,9] such that anti-infection and osseointegration can be achieved simultaneously after implantation.[10] However, the efficacy of this scaffold-based anti-infection strategy is limited by the presence of drug-resistant bacteria and biofilm.[10]

Biofilm is a confluent mixture of bacteria and extracellular polymeric substances.[11] It colonizes preferentially on the implant–bone interface, thus protecting bacteria against phagocytosis and antibiotics, and is directly responsible for the recurrence of infection after treatment.[12] The intractability of the drug-resistant bacteria is mainly caused by the extensive misuse of antibiotics; drug-resistant bacteria tend to compromise the efficiency of antibiotic administration/treatment.[13] Bacteria can also rapidly adjust their metabolic systems to resist newly developed antibiotics.[13,14] The development of implantable porous scaffolds, with antimicrobial activity against bacterial biofilms without the need for antibiotics, has prompted extensive research aimed at improving the outcomes of IBD treatment.[15–17]

New developments in material science have led to advances in IBD treatment.[3,10] As a typical two-dimensional material, reduced graphene oxide (RGO) exhibits excellent osteogenic activity and anti-biofilm capacity, thus making it a promising candidate for anti-infection porous scaffolds.[18–20] More importantly, RGO has the tendency to denature bacterial proteins and deconstruct biofilms via oxygen free radicals produced through contact with bacteria.[21] This oxidative, stress-mediated anti-biofilm activity suggests the potential of RGO to prevent the revival of drug-resistant bacteria in the treatment of traumatic infections. For instance, Das et al fabricated a protein-conjugated RGO composite using a one-pot biosynthetic process; the prepared material exhibited robust antibacterial ability and ideal biocompatibility, which is required for effective anti-infection coatings for implant materials.[22] However, the long-term antibacterial ability of RGO is limited due to the continuous oxidation of its surface.[15] Therefore, to prolong the anti-biofilm activity of RGO, it is necessary to develop a new composite material based on the reduction of GO.

Silver nanoparticles (AgNPs), as a broad-spectrum antibacterial nanomaterial, have attracted much attention with respect to the antibacterial properties afforded by their incorporation into materials.[16,23,24] However, due to a large surface energy, AgNPs are highly susceptible to spontaneous agglomeration,[25,26] resulting in a large loss of antibacterial activity.[25,26] Therefore, in practice, AgNPs are often dispersed in a carrier to minimize clustering.[19,27,28] The two-dimensional sheet structure of graphene serves as a good NP carrier vehicle.[4,22] At present, a variety of AgNP-loaded graphene composite materials have been developed for in vivo and in vitro antibacterial research.[16,19,27,29] However, three-dimensional (3D) porous AgNP-loaded graphene composites for bone tissue engineering scaffolds have rarely been reported.

In our earlier studies, we successfully constructed a 3D porous scaffold based on the self-assembly of RGO and nano-hydroxyapatite (nHA); when loaded with vancomycin, this system facilitates controlled release of antibiotics and promotes osteogenesis and infection control.[4] Based on our earlier study, here we prepared an AgNP-loaded RGO/nHA 3D porous scaffold (AgNPs-nHA@RGO, AHRG) by adding a reducing agent and Ag ions. Methicillin-resistant Staphylococcus aureus (MRSA, ATCC 43,300, USA) was used as the model-resistant bacterium, and the effects of different Ag loadings on antimicrobial activity were studied. In addition, the cytocompatibility of materials was also examined. Finally, the as-fabricated AHRG scaffold was applied to a rabbit IBD model to evaluate its therapeutic effect in vivo.

Materials and Methods

Materials

Ascorbic acid, bovine serum albumin (BSA; standard grade), and sodium glutamate were purchased from Sigma-Aldrich Trading Co., Ltd. (Shanghai, China). nHA was purchased from Aladdin Chemistry Co., Ltd. (Shanghai, China). Expandable graphite flakes were ordered from ChengYang Graphite Products Co., Ltd. (Qingdao, China). Silver nitrate, glacial acetic acid, methanol, ethanol, and a glucose analysis kit were purchased from Sinopsin Group Chemical Reagent Co., Ltd. (Shanghai, China). Crystal violet was purchased from Beijing Solibao Technology Co., Ltd. (Beijing, China). Trypsin soy broth (TSB) and trypsin soy agar (TSA) were purchased from Becton Dickinson Co., Ltd. (Franklin Lakes, NJ, USA). Fetal bovine serum (FBS), penicillin-streptomycin double-antibiotic solution, trypsin, Dulbecco's modified Eagle's medium (DMEM)/F-12, and phosphate-buffered saline (PBS) were

purchased from Gibco (Grand Island, NY, USA). CCK-8 and lactate dehydrogenase (LDH) kits were purchased from Biyuntian Biotechnology Co., Ltd. (Shanghai, China). New Zealand white rabbits were purchased from SLAC Laboratory Animal Co., Ltd. (Shanghai, China). The water used in all experiments was purified using a Milli-Q water purification system (Millipore, Bedford, MA, USA), with a resistivity of 18.2 MΩ cm.

AHRG Scaffold Preparation

The AHRG scaffold was prepared using a modified version of the self-assembly process described in our previous study.[30] For optimal 3D porous morphology and bone repair capacity, the ratio of nHA to GO was fixed at 20% according to our previous investigation.[30] In specific, the detailed preparation process for 1% AHRG is described below. GO (200 mg) was added to 50 mL of ultrapure water and then ultrasonically dispersed for 10 min to obtain a 4 mg/mL GO colloid solution. Subsequently, 40 mg of nHA powder was added to the solution, and ultrasonic dispersion was again performed for 10 min to obtain a 20% nHA@GO precursor solution. Finally, 100 mg of ascorbic acid and 3.15 mg of silver nitrate were added in sequence in an ice water bath under a vigorous stirring speed of 600 rpm. After stirring for 30 min, the mixture was placed in a beaker sealed with foil; the beaker was then placed in a water bath at 80°C to induce self-assembly. After heating in a water bath for 2 h, the precursor mixture formed a separate 3D porous scaffold. At the same time, the colloidal solution became clear and transparent. The silver nitrate was added in the same manner as during the preparation of the 1% AHRG scaffold, to construct 2%, 4%, and 8% AHRG scaffolds.

Characterization of the AHRG Scaffold

The structure and physicochemical properties of the prepared scaffolds were characterized by scanning electron microscopy (SEM) and transmission electron microscopy (TEM). The mechanics and porosity of the prepared scaffolds were examined using an Instron mechanical test system (Instron Corporation, Canton, MA, USA) and the liquid displacement method.[31]

For TEM, to better disperse the nanoparticles throughout the scaffolds, the scaffolds were re-pulverized using a freeze-grinding method. In detail, 50 mg of scaffold was placed in a 5-mL centrifuge tube and blended with 2 mL of ethanol and beads. Subsequently, the centrifuge tube containing the mixture was fixed to the holder of the freeze grinder. After polishing, an appropriate amount of slurry was removed, dropped onto a copper mesh, and allowed to evaporate naturally; TEM was then performed.

Bacterial Culture

Given that drug-resistant Staphylococcus aureus is the main pathogen responsible for refractory osteomyelitis and IBD, MRSA (ATCC 43,300; American Type Culture Collection, Manassas, VA, USA) was selected as the model bacterium to evaluate the antibacterial activity of the prepared scaffold. The collected bacteria were inoculated in a conical flask containing 100 mL of fresh tryptic soy broth (TSB) liquid medium and then placed in a 37°C shaker for 24 h at 100 rpm. After colony amplification, the precipitate was centrifuged, with 10 mL of bacterial preservation solution then added. The pipette was carefully blown, resuspended, and stored at 4°C until further use.

The TSB powder (30 g) was weighed, stirred, and dissolved in 1000 mL of ultrapure water, and then autoclaved at 121°C for 15 min. The preservation solution was prepared by mixing 5% (w/v) sodium glutamate, 5% (w/v) BSA, and ultrapure water in equal amounts. The solution was stirred gently (to avoid foaming) for 20 min, sterilized by filtration through a 0.22-μm filter, and stored at 4°C.

In subsequent antibacterial experiments, TSB solid medium was used, and was prepared by dissolving 20 g of tryptic soy agar (TSA; soybean-casein digested agar) in 500 mL of ultrapure water. The solution was then autoclaved at 121°C for 15 min. After sterilization, the solution was allowed to cool to room temperature and then frozen. Note that the solution can be stored for 6 months at room temperature.

Anti-Bacterial Evaluation

The antibacterial activity of the scaffold was examined by dynamic bacterial proliferation and solid Kirby–Bauer diffusion assays.[32] For dynamic antibacterial experiments, the preserved MRSA was resuscitated using the TSB liquid medium. The resuspended MRSA was inoculated at a density of 2×10^5 cells/mL into a conical flask containing 100 mL of TSB liquid medium, to which the scaffold was added. The bacterial suspension was incubated at 37°C with shaking at 150 rpm. At different time points, 100 μL of the culture

solution was withdrawn using a microsyringe, and the concentration of bacteria in the liquid was analyzed using a cell counter.

For the solid Kirby–Bauer diffusion test, the TSB solid medium was preheated at 60°C and then cast into a Petri dish (10 mL solid medium per dish). After cooling the medium to room temperature, 20 μL of the bacterial suspension (1×10^6 CFU/mL) was added to a culture dish as a uniform coating. At the same time, the AHRG scaffold material underwent ultraviolet radiation sterilization was carefully placed on the center of each dish. Finally, all dishes were incubated at 37°C for 24 h. The diameter of the inhibition zone of each sample was measured by an automatic image processing system (FR-989; Fushi, Shanghai, China).

Bacterial Biofilm Inhibition Experiment

To better induce the growth of bacterial biofilms in vitro, a TSB medium containing 1% (w/v) glucose was used for MRSA resuscitation and culture. Bacteria were resuscitated and diluted 100-fold with the culture solution. Subsequently, the bacterial dilution (3 mL/well) and scaffolds (Sterilized with ultraviolet radiation) to be tested were added sequentially to a six-well cell culture plate. After incubation at 37°C for 24 h, the scaffold and medium were discarded, and the well was washed three times with PBS and fixed by methanol for 20 min. Afterwards, excess methanol was aspirated, 1% crystal violet staining solution was added, and the mixture was incubated at room temperature for 10 min. The unbound crystal violet was washed with distilled water and allowed to dry naturally. After the well plate had dried completely, 2 mL of 33% glacial acetic acid solution was added to each well and maintained at 37°C for 30 min to dissolve the crystal violet. Finally, the optical density (OD) of each well of the plate was measured at 590 nm using an automated microplate reader. Considering background absorbance, the OD of the blank plate was subtracted from the calculated value.

In vitro Cell Compatibility Assay

The in vitro cytocompatibility of the scaffold was examined using rat bone marrow stromal cells (rBMSCs). Specifically, rBMSCs from 1-week-old female rats were harvested and cultured following a previously reported method.[33] Rats were sacrificed, the femoral cavities were exposed, and the marrow cavity was rinsed with FBS (10%) (Gibco; Thermo Fisher Scientific, Waltham, MA, USA) in PBS (Hyclone, Logan, UT, USA). The cells were flushed out and collected. After centrifugation at 1000 rpm for 10 min, the cell suspension was resuspended in DMEM/F12 (Hyclone) containing 15% FBS, 100 U mL^{-1} penicillin (Gibco, Grand Island, NY, USA), and 100 mg mL^{-1} streptomycin (Gibco). Subsequently, a cell culture flask was applied for cell seeding in a humidified atmosphere with 5% CO_2 at 37°C. Once the rBMSCs had been passaged three times, they were used in the following experiments.

In this study, the rBMSC suspension was seeded in 96-well plates at a density of 3000 cells per well. After 24 h of culture, the adherent cells in the well plates were treated with different concentrations (10, 20, 40, 80, 160, 320 μg/mL) of AHRG scaffold. The tested scaffold samples were sterilized with ultraviolet radiation for 3 h before use. After 1 and 3 days of incubation, cell viability and damage were assessed by CCK-8 and LDH kits, according to the manufacturer instructions. Finally, the measured values were normalized, taking the OD value of the normal control group as 100%.

In vivo Evaluation

All animal studies were conducted at the Animal Experimental Center of the Naval Military Medical University (Shanghai, China). All animals were maintained on a standard sterile diet. The breeding room was kept under constant temperature and humidity conditions (23–25°C and 40–70%, respectively) with a computer-controlled 12-h/12-h light/dark cycle. The animal surgical protocols were conducted according to the NIH guidelines for the care and use of laboratory animals (NIH Publication No. 85–23 Rev. 1985) and was assessed and monitored by the Changhai Hospital Laboratory Animal Ethics Committee to ensure that all animals were treated humanely and appropriately during the study.

Forty-five male New Zealand rabbits (average body weight: 3 kg) were randomly divided into three groups: an untreated group, a 20% nHA@RGO implant group, and a 4% AHRG implant group. Before model establishment, 0.5 mL of blood was collected from the marginal ear veins for leukocyte and C-reactive protein (CRP) measurement, with the values obtained used as the baseline values. After preparing the right forelimb for disinfection with iodophor, the rabbits were anesthetized with 5% isoflurane gas, and a longitudinal incision 1.5 cm in

length was made along the anteromedial aspect of the forelimb. The vessels and muscles were bluntly separated to expose the radius bone. An oscillating saw (Stryker Cooperation, Kalamazoo, MI, USA) was used to remove a 10-mm segment from the middle of the radius shaft. After irrigation of the bone void with saline solution, 0.5 mL of a saline suspension, with a MRSA concentration of 2.5×10^6 CFU per mL, was injected into the defect site and the bone marrow cavity. Sodium morrhuate (0.2 mL) (Xinyi Jinszhu Pharmacy Co. Ltd, Shanghai, China) was then added, and sterilized medical bone wax (B. Braun Surgical, Aesculap Ag & Co., Germany) was used to seal the cavity. The incision was closed with #1 stitches (Ethicon, Somerville, NJ, USA).

After surgery, the degree of bacterial infection was determined based on indicators such as body weight, blood leukocytes, and CRP. After 2 weeks, the scaffolds were implanted into the defect site following lavage and debridement. The scaffold were sterilized with ultraviolet radiation for 3 h before use. The animals were closely observed for changes in body weight, white blood cell (WBC) count, and CRP level. Bone regeneration was assessed by micro-computed tomography (micro-CT, SkyScan 1076; Bruker, Ettlingen, Germany). Then, 3D CT images were reconstructed using SkyScan CTVOX 2.1 software (Bruker), and bone mass (BV) and bone mineral density (BMD) were analyzed.

Histological Analysis

Further insight into the microstructure of the regenerated bone was achieved by histological analysis. The harvested forearm bone specimens obtained from the sacrificed rabbits at 8 and 12 weeks after implantation were fixed overnight in 4% paraformaldehyde, dehydrated in a graded series of ethanol (70%, 75%, 80%, 85%, 90%, 95%, and 100%) for 24 h, and embedded in polymethylmethacrylate (Sinopharm, Beijing, China). Serial sagittal sections (thickness: 100 μm) were obtained using a microtome (EXAKT 310; Exakt Technologies, Oklahoma City, OK, USA) and then polished to a thickness of 40 μm. Sections of the undecalcified specimens were then subjected to hematoxylin and eosin (H&E) and Toluidine blue (T-blue) staining and observed under a light microscope (TE2000U; Nikon, Tokyo, Japan) to assess new bone regeneration. The tissue slices were dewaxed with xylene, rehydrated using decreasing concentrations of ethanol, and washed in PBS before staining. For H&E staining, the slices were resined with H&E and dried. For T-blue staining, the slices were soaked in T-blue liquid for 30 min, placed in an acetic acid solution, washed with water, and then air-dried.

Statistical Analysis

All quantitative data are expressed as means ± standard deviation (SD). Statistical analysis (one-way analysis of variance) was performed using Origin 9.0 software (OriginLab Corporation, Northampton, MA, USA). A p-value < 0.05 was considered statistically significant.

Results and Discussion

Synthesis and Characterization of the AHRG Scaffold

Figure 1 shows a flow diagram of the scaffold design and preparation. First, different proportions of precursor materials were mixed together to form a homogeneous colloidal solution. Subsequently, GO was reduced to RGO by ascorbic acid to form a 3D porous scaffold. At the same time, Ag ions underwent a transformation, resulting in AgNP formation. Finally, the AgNPs were loaded onto the RGO 3D porous scaffold together with nHA to obtain an AHRG scaffold. To improve the antibacterial ability of the prepared scaffold, AgNPs were used to functionally modify the scaffold. According to previous reports, GO has a strong ability to adsorb Ag ions.[34–36] Moreover, under certain reducing conditions, GO can induce Ag ions to grow directly on its surface, thereby forming RGO AgNP composites.[16,29,34] Thus, for smooth and uniform loading of AgNPs onto the scaffold, we used an in situ reduction method to induce the RGO scaffold, with biocompatible cochroic acid employed as the reducing agent. AgNPs were also formed during the reduction-assembly process.

Figure 2 shows SEM images of the surface morphology of the materials. The prepared scaffold had a three-dimensional porous structure. In General, the pores were clear, and the pore wall structure was relatively complete and the granule like AgNPs (Figure S1) were observed attached to the scaffold surface. The distributions of pore size of different scaffolds were depicted in Figure S2. We found that although all the 1%, 2%, 4%

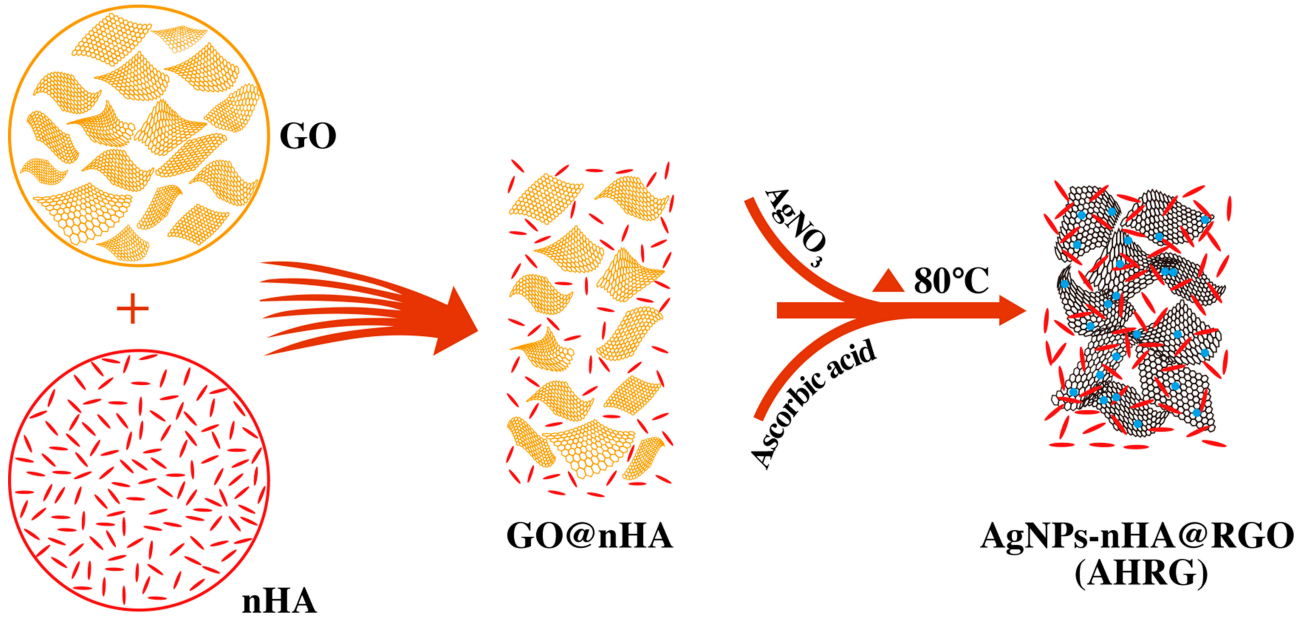

Figure 1 Schematic showing that the self-assembly of GO, nHA and $AgNO_3$ to form a porous AHRG scaffold.

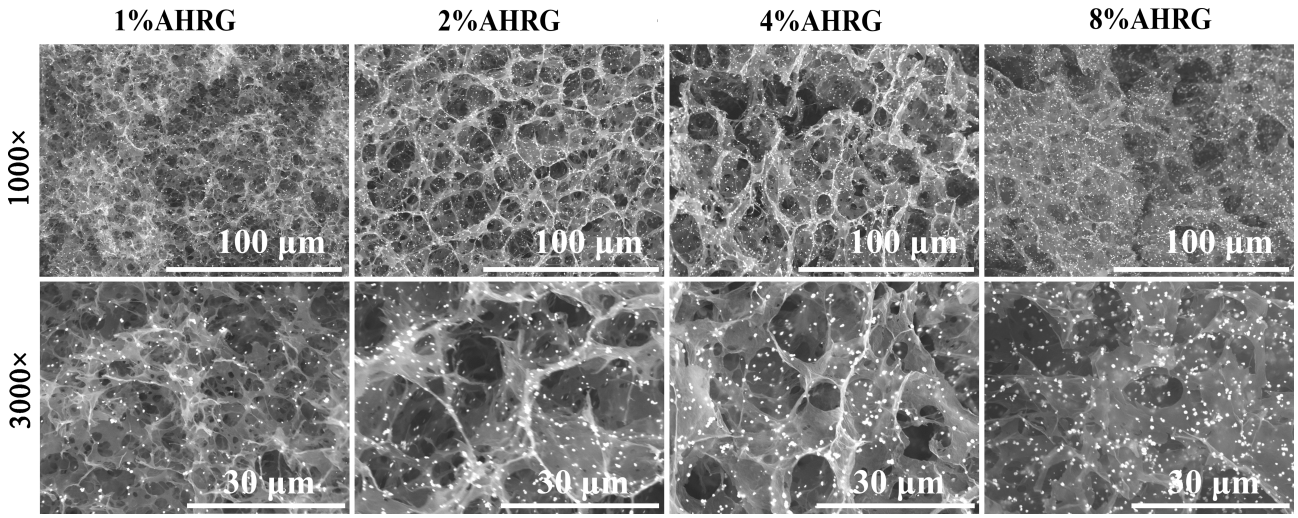

Figure 2 SEM analysis of the AgNPs-nHA@RGO (AHRG) scaffold with the different AgNPs loading ratios.

and 8% AHRG have 3D porous structure, the pore sizes of 2% and 4% AHRG were slightly larger. In specific, when the concentration of AgNP doping increased to 8%, some pore walls collapsed according to the SEM observation, and the pore size was slightly reduced compared with 2% and 4%. The general morphology was similar to the 20% nHA@RGO.[30] The interconnected porous structure can facilitate bone growth and such construction will not be compromised by a rational concentration of AgNP doping.

The AgNP distribution was uniform, and the density increased with the amount of Ag ions added during preparation. This linear growth relationship also indicates that the high conversion efficiency of Ag ions to AgNPs was reduced during the self-assembly process. To verify this, the Ag ion content of the transparent solution was examined after formation. Following self-assembly, the concentration of Ag ions in the solution corresponded to only 15–20% of the initial amount added (Table 1). These results showed that, in this system, Ag ions were converted at a rate exceeding 80%. Based on previous studies, we know that silver nitrate can be reduced to nanosilver, i.e., AgNPs, according to a conversion efficiency exceeding

Table 1 Silver Ion Concentration Before and After Self-Assembly

Group	Ag^+ Concentration Before Reaction (μg/mL)	Ag^+ Concentration After Reaction (μg/mL)	Conversion Rate (100%)
1% AHRG	61.52 ± 5.39	8.96 ± 1.57	85.4
2% AHRG	118.36 ± 9.85	22.97 ± 3.86	80.6
4% AHRG	231.83 ± 12.67	43.96 ± 6.79	81.0
8% AHRG	493.45 ± 16.55	96.86 ± 11.35	80.4

80%.[16,28,37] Therefore, the graphene material in this study was not only the principle component with respect to self-assembly, but was also a major contributor to the improved formation efficiency and dispersion of AgNPs.

To further confirm the formation of AgNPs in the scaffold, we analyzed the valence and structure of elemental Ag therein using X-ray photoelectron spectroscopy (XPS). The structure and composition of AgNPs in the scaffold were then further analyzed by selected area electron diffraction (SAED). Due to interference by nHA, the correlation spectrum of AgNP in the scaffold could not be accurately obtained by X-ray diffraction. TEM was used to resolve the structure of AgNP in the scaffold in more detail. Because nHA is a fusiform structure, our focus in this study was mainly on spherical AgNPs; the results are shown in Figure 3A and B. The concentric diffraction ring of the high-resolution image indicates that the AgNPs were polycrystalline. The parameters of the diffraction ring were consistent with standard AgNP crystal surface parameters. Subsequent high-resolution images, in which the crystal plane parameter of 0.234 nm

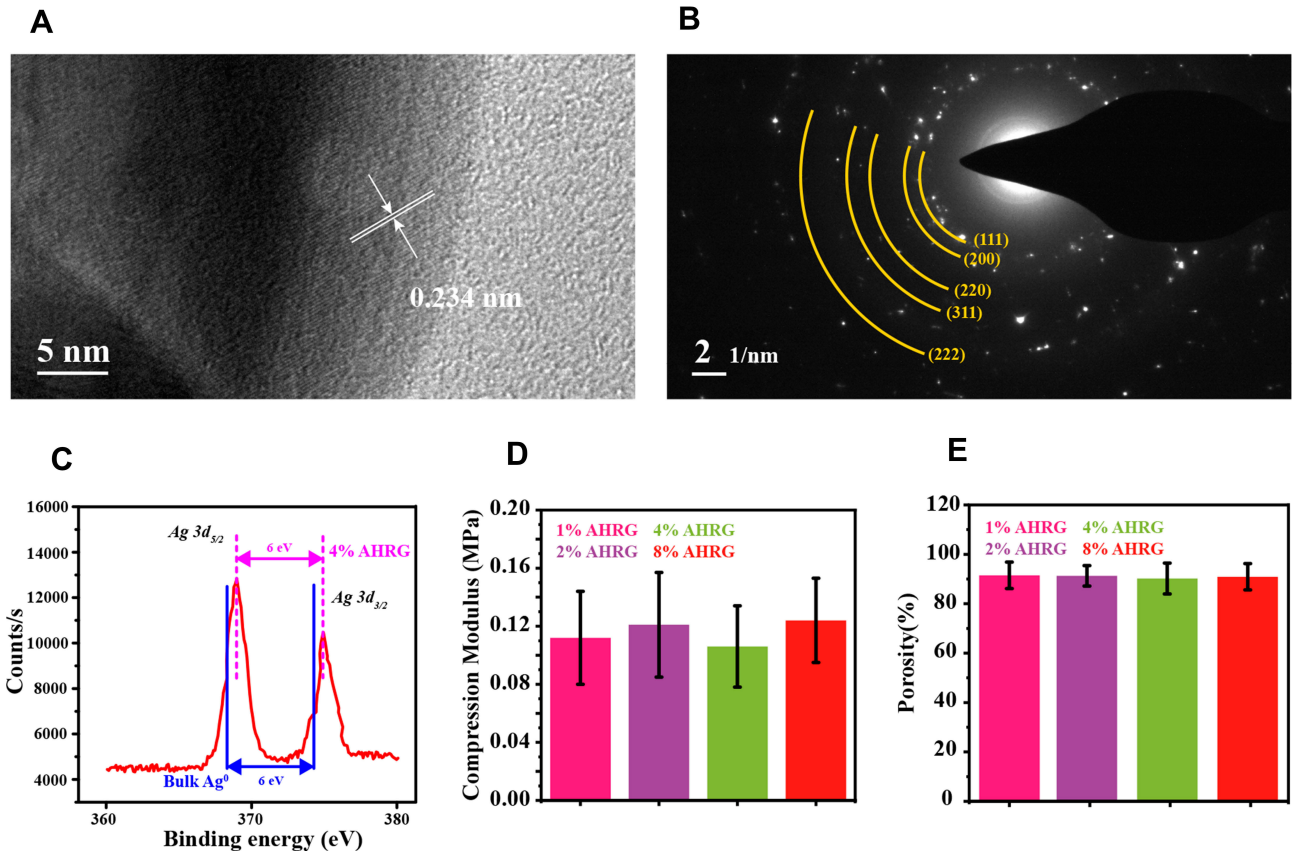

Figure 3 Physicochemical characterization of AHRG scaffolds, (**A**) High-resolution transmission electron microscopy, (**B**) Selected area electron diffraction, (**C**) X-ray photoelectron spectroscopy, (**D**) compressive modulus of each set of scaffolds, (**E**) Porosity of each set of scaffolds.

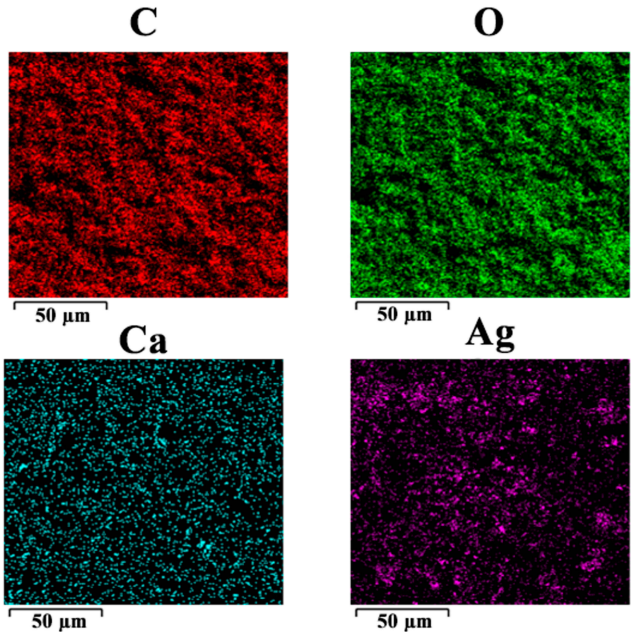

Figure 4 EDS mapping of the cross section of the scaffold.

corresponds to the nano-silver (111) crystal plane, confirmed the diffraction results. The 368.3 and 374.3 eV absorption peaks appearing in the XPS pattern in Figure 3C are the binding energies of the Ag 3d5/2 and Ag 3d3/2 electronic states, respectively. Given that the Ag 3d5/2 and Ag 3d3/2 electron binding energies of standard zero-valent Ag are 367.9 and 373.9 eV, respectively, the elemental Ag in the prepared scaffold did not appear to have a single binding energy. We found that the difference in binding energy between the two Ag electronic states in the scaffold was equal to that of standard elemental Ag, i.e., zero-valent Ag. The change in overall electron binding energy indicated that the supporting effect of AgNP and graphene on the scaffold was greater than that conferred by physical adsorption. Based on the results of previous studies, we speculate that this result may be related to the in situ growth of AgNP on graphene.[19,27] In summary, the structure and morphology of AgNPs, as observed in SEM images, were confirmed by XPS and SAED.

For the treatment of infected bone defects, the mechanical properties of the scaffold as bone substitute are very important parameters. In our previous study, we found that the mechanical properties of nHA@RGO scaffold with 20% nHA were relatively ideal.[30] In this

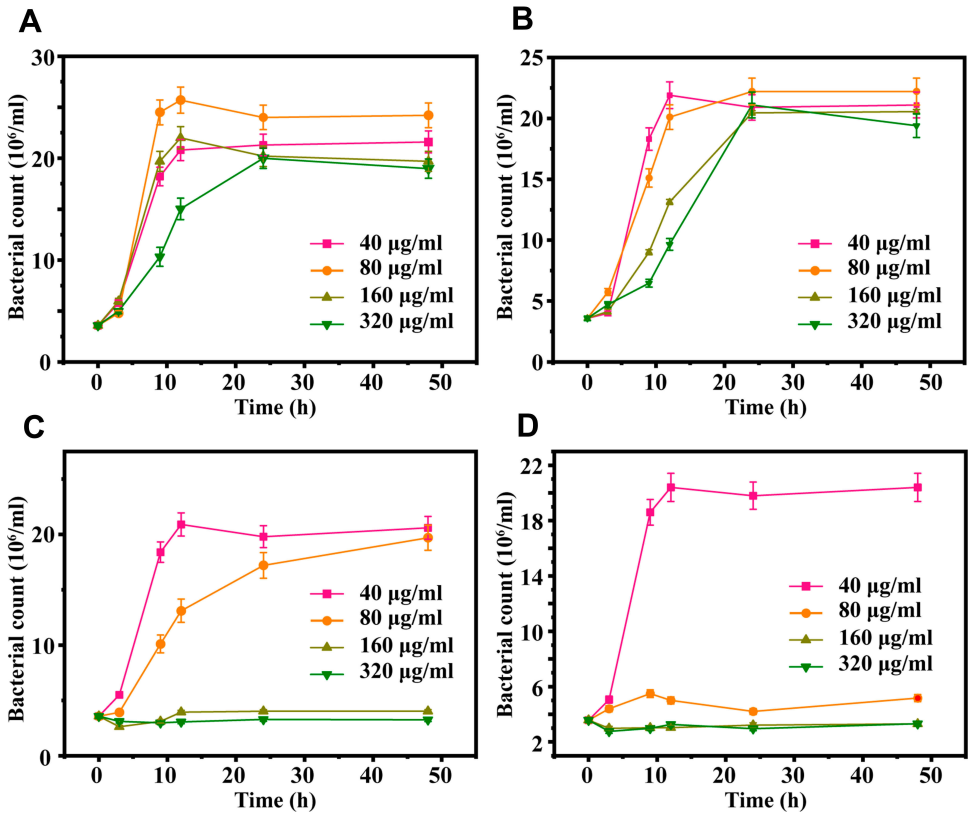

Figure 5 Antibacterial curve of different nano-silver loading AHRG scaffolds, (**A**) 1% AHRG, (**B**) 2% AHRG, (**C**) 4% AHRG, (**D**) 8% AHRG.

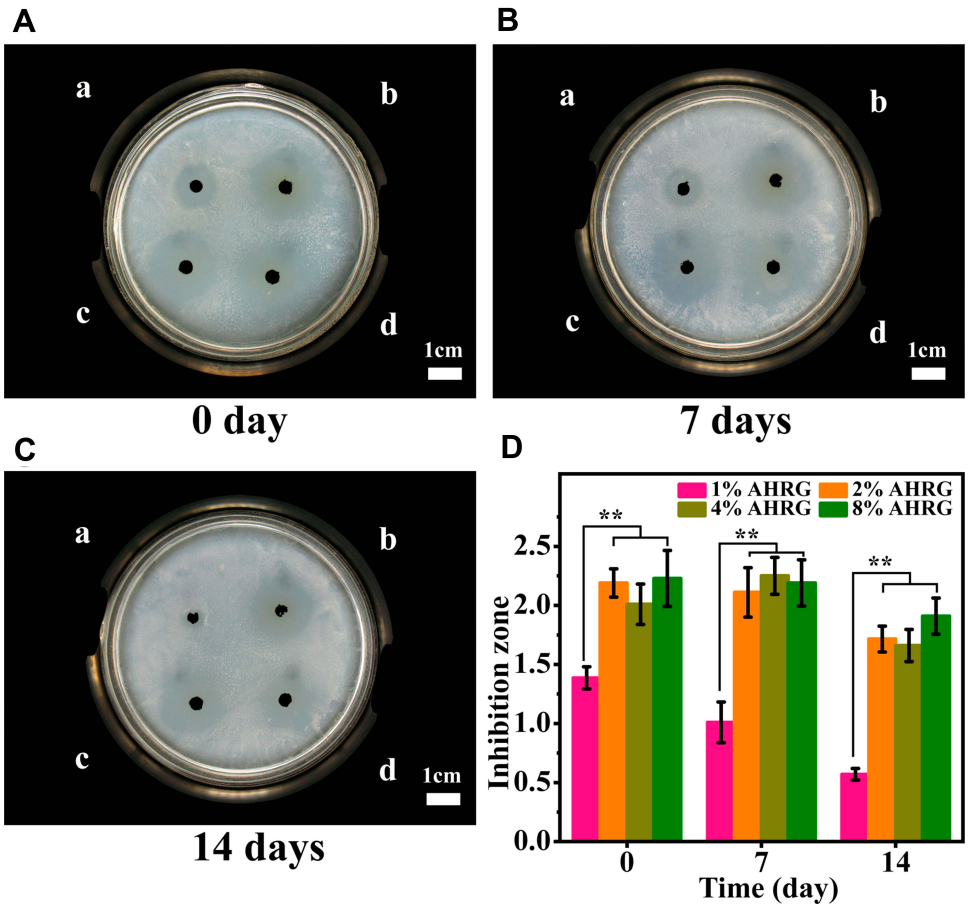

Figure 6 Kirby-Bauer diffusion test of different nano-silver loading AHRG scaffolds, (**A**) Original untreated AHRG scaffold, (**B**) Scaffold soaked in PBS for 7 days, (**C**) Scaffold soaked in PBS for 14 days, and (**D**) Statistical graphs of inhibition zone diameters for each AHRG scaffold. Label a, b, c, and d represent 1%, 2%, 4%, and 8% AHRG scaffolds, respectively. **p <0.01.

study, we studied the mechanical properties of 20% nHA@RGO with different AgNP doping concentration, such as compressive modules module and scaffold porosity. As shown in Figure 3D, with concentrations of AgNP doping varied, the compressive modules module of the scaffolds changed, but there was no significant difference among them. In addition, the porosity of the scaffold is also an important indicator to evaluate whether it can effectively promote bone growth. As shown in Figure 3E, the porosity of all AHRG scaffolds reached about 90%, indicating high porosities. The above two parameters are similar to the data measured in 20% nHA@RGO in our previous study.[30]

Electron diffraction spectroscopy was used to examine the element distributions in the scaffold's cross-section; the results in Figures 4 and S3 show that the element distributions before and after the scaffold reaction were basically consistent with those of the nHA@RGO scaffold reported in our earlier study.[30,38] Ag, carbon, calcium, and phosphorus were distributed uniformly throughout the scaffold's cross-section. A heterogeneous distribution of AgNPs and nHA throughout the scaffold was also seen. The above results indicated successful preparation of AHRG 3D porous scaffolds at a lower temperature via an improved self-assembly method.

Antibacterial Activity

In this study, antibacterial properties were among the major functions of interest of the prepared scaffolds. To verify the antibacterial properties of the scaffold in detail, three evaluation approaches were applied: dynamic antibacterial evaluation, solid Kirby–Bauer diffusion tests, and biofilm inhibition evaluation. In the dynamic antibacterial experiment, inhibition curves of different AHRG scaffold concentrations were generated, and the minimum bactericidal concentration (MBC) and minimum inhibitory concentration (MIC)

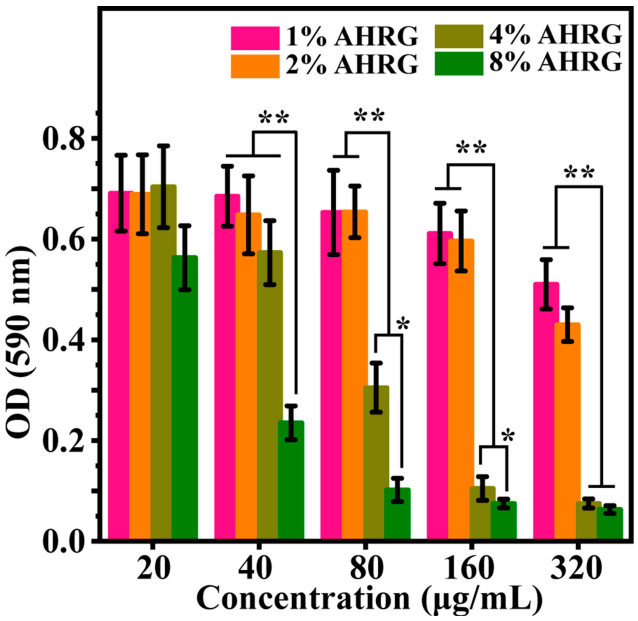

Figure 7 Growth of MRSA biofilm after treatment with different AHRG scaffold. *p <0.05, **p <0.01.

were calculated. The Kirby–Bauer experiment provided additional evidence of antibacterial activity and was also used as an indicator of the degree of antibacterial activity of the fabricated scaffolds. Biofilm formation is one of the most important causes of various intractable infections, as well as bacterial resistance.[11,12,39] A better theoretical basis for subsequent animal experiments can be obtained by studying the biofilm inhibitory activity of scaffolds.

Figure 5 shows the results of dynamic antibacterial experiments on different scaffolds. The MIC against MRSA treated with a 1% AHRG scaffold was 320 μg/mL; no significant bactericidal effect was evident within the concentration range tested. The MIC of 2% AHRG was less than that of the 1% AHRG scaffold (160 μg/mL). However, similar to 1% AHRG, 2% AHRG also showed no bactericidal effect within the concentration range tested. When the loading of AgNPs reached 4%, the MIC dropped still further, to 80 μg/mL. It is worth noting that in the antibacterial growth curve of 4% AHRG, complete inhibition of bacterial growth and obvious bactericidal effects were observed. The MBC of 4% AHRG was 160 μg/mL; 8% AHRG also showed complete inhibition of bacteria, and its MBC continued to decrease, reaching 80 μg/mL. This experiment showed that as AgNP loading increased, the antibacterial capacity of the scaffolds continued to improve. Higher AgNP loading clearly showed better antibacterial activity. When the loading of AgNPs exceeded 4%, the bactericidal effect of the material became evident, manifested in a flat bacterial growth curve for the 4% and 8% AHRG scaffolds.

The results of the solid Kirby–Bauer diffusion test are shown in Figure 6. The appearance of the inhibition zone indicated that all of the scaffolds showed antibacterial activity to some degree. The diameter of the inhibition zone was measured as a quantitative index of the strength of the AHRG antibacterial capacity. Figure 6 shows that the diameter of the inhibition zone increased with AgNP loading. However, similar to the results of the dynamic antibacterial experiment, when AgNP loading exceeded 4%, the area of the scaffold inhibition zone did not change significantly. The persistence of the antibacterial effects of the scaffolds was investigated in solid-state plate diffusion experiments. Figure 6B and C show the inhibition zone of the scaffolds soaked in PBS for 7 and 14 days, respectively; the antibacterial activity of all scaffolds decreased after prolonged immersion in PBS. The diameter of the inhibition zone of 8% AHRG decreased from 2.34 ± 0.26 cm to 1.73 ± 0.16 cm. Similarly, the inhibition zone diameter of 4% AHRG decreased from 2.03 ± 0.19 cm to 1.63 ± 0.14 cm. The 2% AHRG group decreased from 2.21 ± 0.25 cm to 1.65 ± 0.11 cm. With 1% AHRG, the diameter of the inhibition zone decreased from 1.35 ± 0.13 cm to 0.48 ± 0.036 cm, effectively indicating a complete loss of antibacterial activity. Relatively, 2%, 4%, and 8% AHRG scaffolds have longer-lasting antibacterial effects. Interestingly, in the experiment of Ag^+ ion release profile from the AHRG scaffold, we found that due to the three-dimensional porous structure and π - π interaction between AgNP and RGO, Ag^+ ion showed an excellent controlled-release profile up to more than three weeks (Figure S4). Based on this result, together with the antibacterial activity, it can be deduced that AHRG is a good sustained-release construction for antibacterial applications.

Figure 7 shows the biofilm inhibition results for the scaffold material. As the amount of scaffold added increased, the OD of all samples gradually declined. However, increased loading of Ag ions inhibited biofilm formation to some degree. For example, the 1% and 2% AHRG treatment groups showed a decline in OD values above 160 μg/mL, compared to the controls.

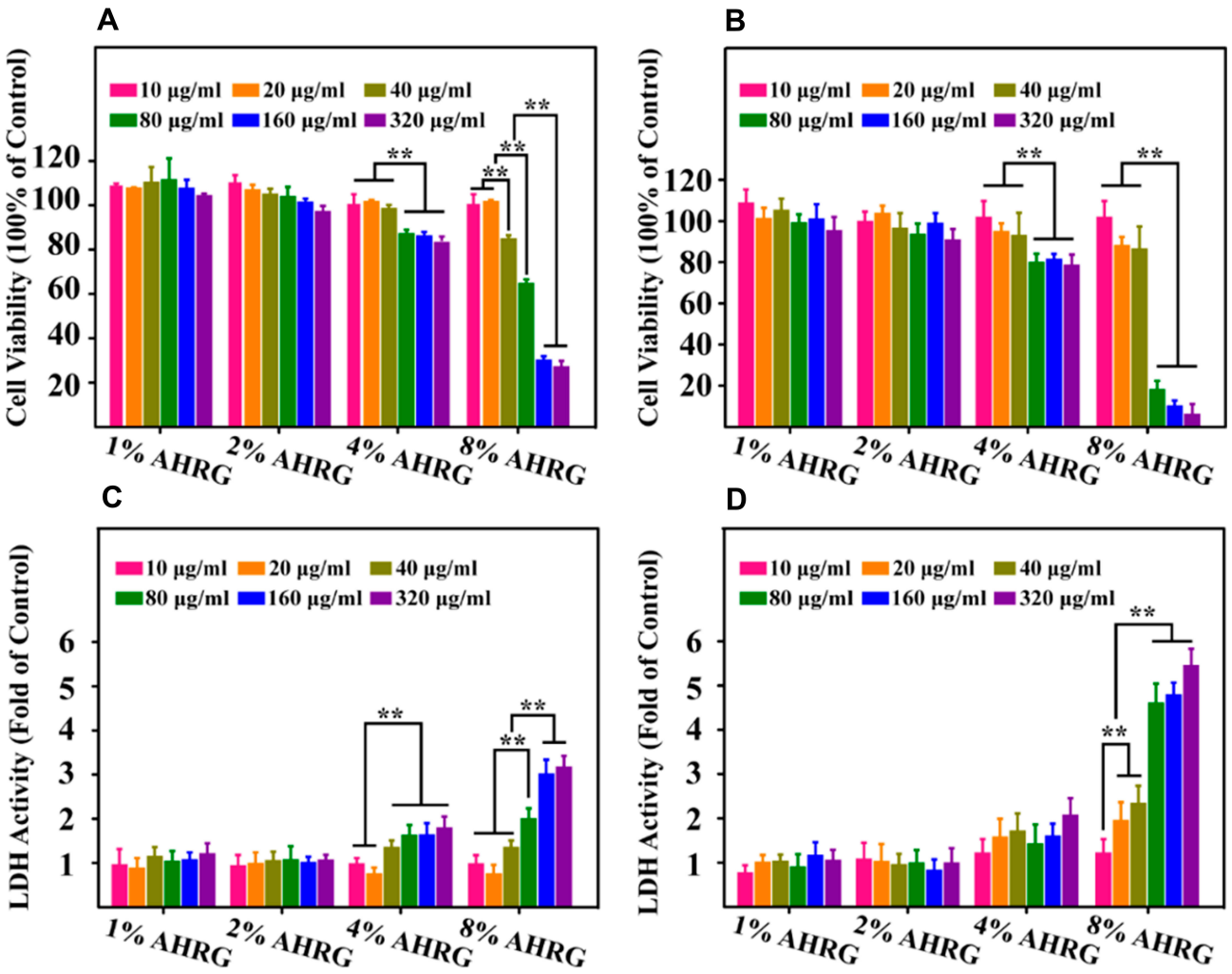

Figure 8 Cell biocompatibility of different AHRG scaffolds, (**A**) Day 1 of CCK-8 test, (**B**) Day 3 of CCK-8 test, (**C**) Day 1 of LDH test, (**D**) Day 3 of LDH test. **p <0.01.

The OD values of the 4% and 8% AHRG groups decreased at relatively low concentrations. The experimental results regarding biofilm inhibition indicated excellent antibacterial performance for the 4% and 8% AHRG scaffolds.

Cell Viability and Cytocompatibility

Figure 8A shows the results of the CCK-8 assay. Cells treated with 1% and 2% AHRG scaffolds showed activity exceeding 90% in after 24 h of incubation, indicating ideal cytocompatibility. For the 4% AHRG scaffold, the concentration decreased after exceeding 40 μg/mL; however, the activity of the cells exceeded 85%. For the 8% AHRG scaffold, a significant decrease in cell viability occurred after reaching a certain concentration. At concentrations above 80 μg/mL, the viability of the scaffold decreased gradually from 65% to 30%, indicating significant toxicity. On the third day of CCK-8 (Figure 8B), the trend similar to that of the first day can be observed.

The LDH experiment validated the CCK-8 results. LDH is an inherent enzyme in cells; when cells become damaged, a certain amount of LDH will be released.[40] Figure 8C and D show the LDH concentration in the supernatant after rBMSCs were treated with scaffolds for 24 and 48 h, respectively. No significant changes were observed in the 1% or 2% AHRG scaffold groups compared to the control group. For the 4% AHRG scaffold, a small amount of LDH was released at concentrations above 40 μg/mL, indicating that the material was toxic to the cells. Cells treated with the 8% AHRG scaffold showed high LDH concentrations (above 40 μg/mL), indicating a strong cytocidal effect. Thus, when the AgNP loading exceeded 4%, the cytocompatibility

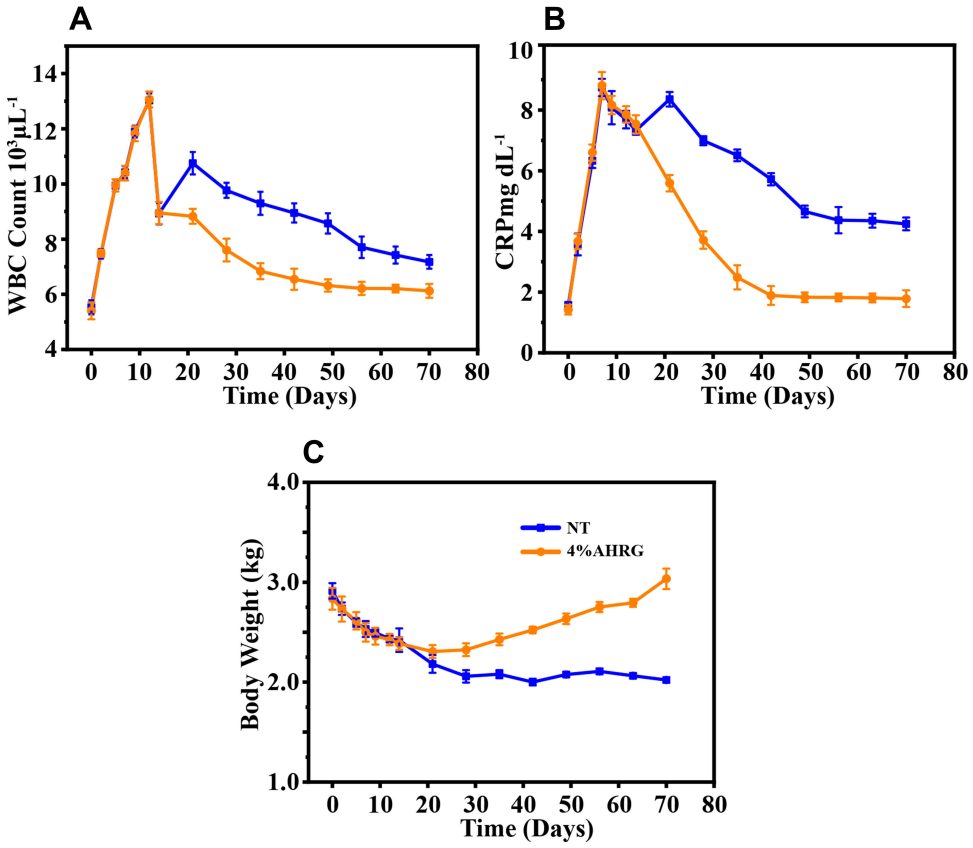

Figure 9 Changes in WBC, CRP, and body weight in rabbits after bacterial injection and material implantation. (**A**) WBC curve, (**B**) CRP curve, (**C**) Body weight curve. The entire experiment was carried out for 70 days. From day 10, the AHRG material was implanted for treatment.

of the scaffold decreased gradually, and toxicity was observed. Combined with the results of the antibacterial experiments, the 4% AHRG scaffold demonstrated good antibacterial activity and relatively good biocompatibility. As such, the 4% AHRG scaffold was subjected to in vivo evaluation.

Repair of Infected Bone Defects in vivo

After physicochemical, in vitro antibacterial, and cytocompatibility assessments, the efficacy of the AHRG scaffold in the treatment of IBDs in a rabbit model was evaluated. After 10 days, the occurrence of IBDs in the animals was verified; the results are shown in Figure 9. All groups of animals showed a significant increase in WBC counts and CRP levels, indicating an inflammatory state. These results showed that the rabbit IBD model was constructed successfully using the aforementioned in situ bacterial inoculation method.

Ten days after the injection of bacteria, the scaffold was implanted. Higher WBC and CRP levels were detected due to the inflammatory response after surgery. However, over time, inflammatory indicators in the 4% AHRG implant group decreased gradually and returned to the normal range within 5 weeks after implantation. The WBC and CRP levels of the untreated group remained higher than those of the normal group. The weight of the rabbits, measured weekly after scaffold implantation, is shown in Figure 9C. During the first week of treatment, a decrease in body weight was detected in all groups due to postoperative inflammation and pain. However, the body weight of the 4% AHRG-implanted group showed a gradual recovery, beginning during treatment week 5. In contrast, in the untreated group, the weight loss was not effectively rescued.

Micro-CT scans were performed at 4, 8, and 12 weeks after implantation (Figure 10A). The untreated group showed the slowest rate of bone bridging and regeneration, with no significant new bone formation until 8 weeks, mainly because of the degree of osteonecrosis and destruction of the osteogenic microenvironment due to bacterial colonization. The rate of bone regeneration in the nHA@RGO group was slightly higher than that in the untreated group, but remained relatively low. Although nHA@RGO has good

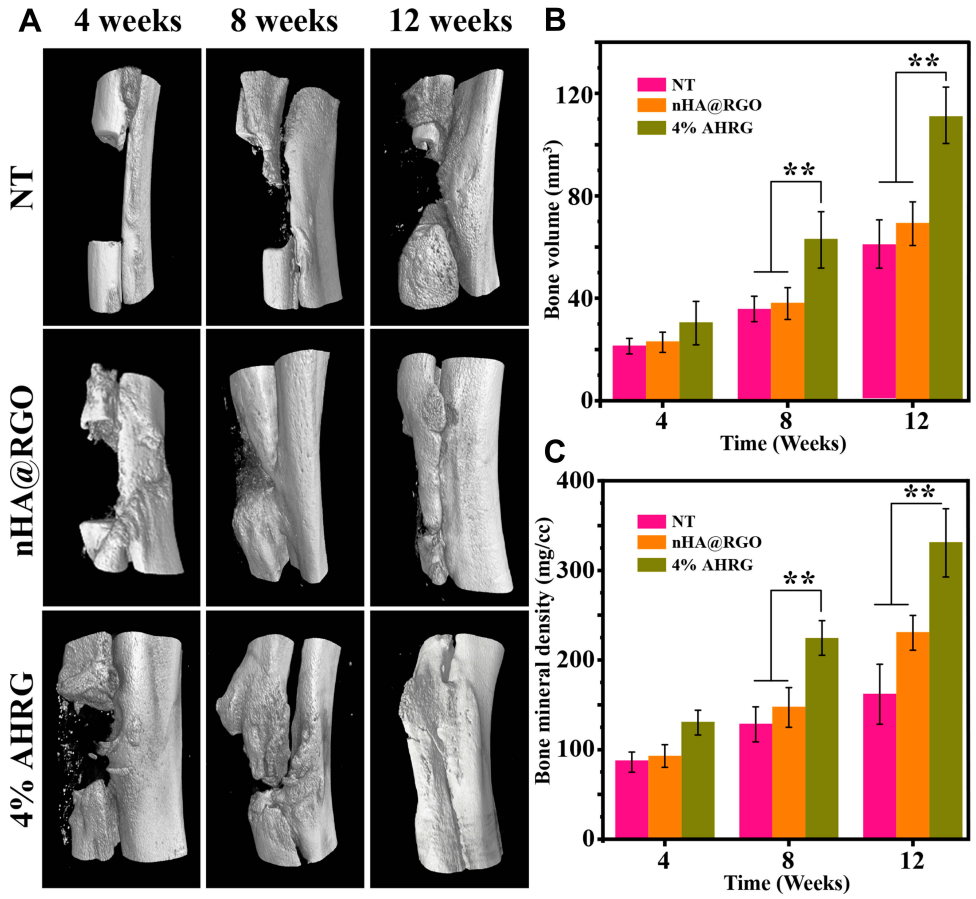

Figure 10 Bone morphology examination of defect repair at different time points after implantation of AHRG material. (**A**) Micro CT 3D reconstruction image of the defect site, corresponding (**B**) Bone volume, and (**C**) Bone density data statistics. **p <0.01.

osteogenic capacity, inflammation caused by infection severely impedes bone regeneration. However, the 4% AHRG scaffold showed better bone repair capacity. This is mainly due to the loading of the scaffold with AgNPs, which greatly improve the antibacterial properties thereof, such that bone repair was accelerated while minimizing the likelihood of infection. The degree of repair of the defect site was analyzed quantitatively in accordance with the BV and BMD (Figure 10B and C). During treatment weeks 4, 8 and 12, although the BV and BMD of the 20% nHA@RGO group increased to some extent, the BV and BMD values observed in the 4% AHRG scaffold were significantly higher than those for the untreated group and 20% nHA@RGO.

Histological and cytological evidence of repair at the defect site was obtained by histological analysis of H&E and TB staining. Figure 11 shows hard, undecalcified sections at 8 and 12 weeks after scaffold implantation. H&E staining results indicated continuous inflammatory cell infiltration during weeks 8 and 12 after surgery in the untreated group. In the nHA@RGO group, although a small number of trabecular structures were observed, a large number of inflammatory cells were also present in the vicinity of new trabecular bone. For the 4% AHRG group, tissue inflammation had subsided considerably at 8 weeks after treatment, and new trabecular bone with intact morphology was observed at week 12.

TB staining provides more compelling histological evidence for new bone formation. At 8 and 12 weeks after implantation, stained sections from the 4% AHRG group showed additional new bone tissue. Also, compared to the nHA@RGO group, the amount of residual black material in the defect site was also substantially reduced (Figure 11B).

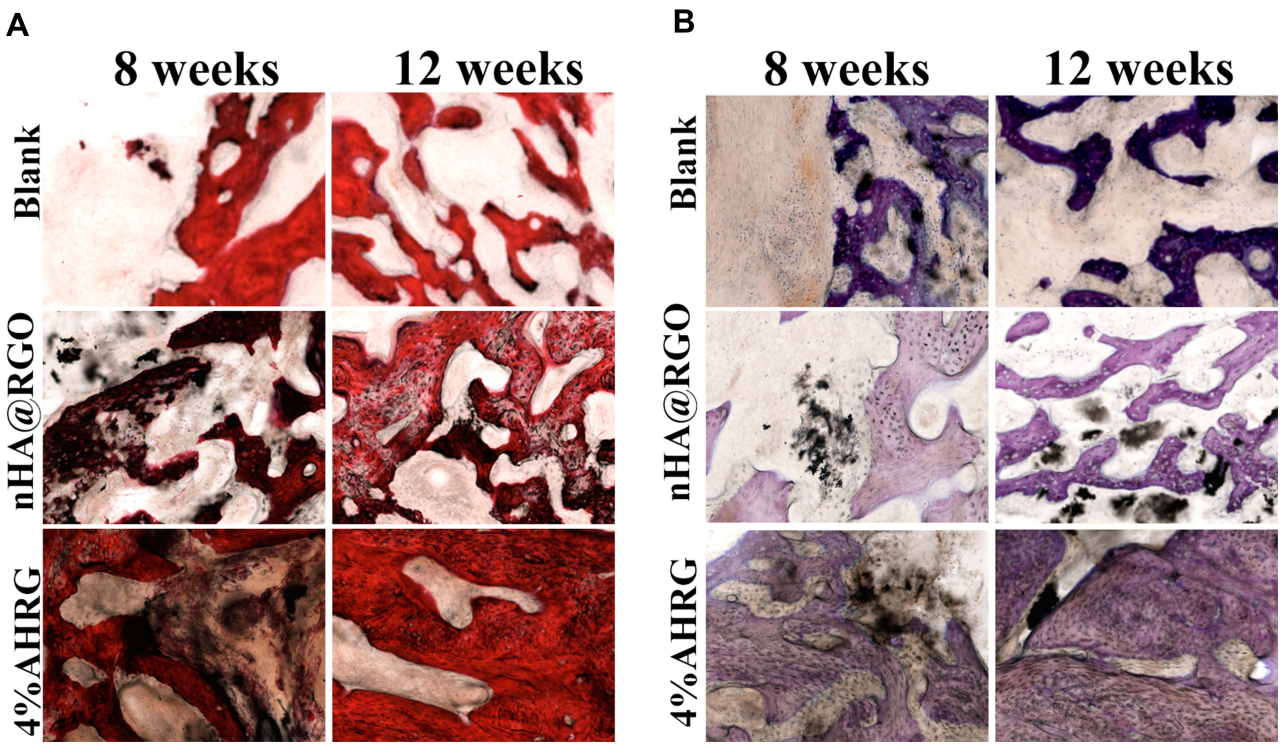

Figure 11 Histological analysis of the defect sites in different experimental groups at different time points: (**A**) HE staining, (**B**) TB staining.

These histological results indicate that the 4% AHRG scaffold has better antibacterial activity than the nHA@RGO scaffold, and is effective in IBD treatment.

Conclusion

Using ascorbic acid as a reducing agent, in the presence of GO, nHA, and Ag ions, a nano-hydroxyl loaded with AgNPs was prepared in one step using a self-assembly method. Physicochemical characterization revealed that the number of Ag ions incorporated was positively correlated with the density of the AgNPs supported on the scaffold. However, AgNP incorporation did not have a significant effect on scaffold topography.

The loading of AgNPs in the composite scaffold greatly enhanced its inhibitory effect on MRSA. The results showed that, when the AgNP content in the composite scaffold reached 4%, the scaffold exhibited the strongest antibacterial activity, and relatively ideal cell compatibility.

The scaffold with 4% AgNP-loaded nHA/RGO (4% AHRG) significantly reduced the levels of inflammatory markers, such as leukocytes and CRP, after implantation in the infected site. In subsequent observations, the healing of the IBD in the implanted group was significantly improved compared to the untreated group. Thus, our results suggest the potential utility of as-prepared AHRG scaffolds for treating of IBDs.

Abbreviations

AgNP, silver nanoparticle; nHA, nano-hydroxyapatite; RGO, reduced graphene oxide; GO, graphene oxide; AHRG, silver nanoparticle (AgNP)-loaded nano-hydroxyapatite (nHA)@ reduced graphene oxide; IBD, infected bone defect; MRSA, methicillin-resistant Staphylococcus aureus; SEM, scanning electron microscopy; TEM, transmission electron microscopy; TSB, trypsin soy broth; TSA, trypsin soy agar; LDH, lactate dehydrogenase; OD, optical density; WBC, white blood cell; CRP, C-reactive protein; H&E, hematoxylin and eosin; T-blue, toluidine blue; XPS, X-ray photoelectron spectroscopy; SAED, selected area electron diffraction.

Acknowledgments

This study was financially supported by the National key research and development plan (2018YFC2001500), Municipal Human Resources Development Program for Outstanding Leaders in Medical Disciplines in Shanghai (2017BR011), Science and Technology Support Project in Biomedical Field of Shanghai Science and Technology Innovation Plan (18431902300), Fundamental Research

Project of the Science and Technology Commission of Shanghai Municipality (15411950600), Shanghai Natural Science Foundation (19ZR1478100), China Postdoctoral Science Foundation (2018M633710), and the China Postdoctoral Special Funding program(the 12th batch).

Disclosure

The authors declare no competing interests in association with this work.

References

1. Bhattacharya R, Kundu B, Nandi SK, Basu D. Systematic approach to treat chronic osteomyelitis through localized drug delivery system: bench to bed side. *Mater Sci Eng C Mater Biol Appl*. 2013;33:3986–3993. doi:10.1016/j.msec.2013.05.036
2. Cheng T, Qu H, Zhang G, Zhang X. Osteogenic and antibacterial properties of vancomycin-laden mesoporous bioglass/PLGA composite scaffolds for bone regeneration in infected bone defects. *Artif Cells Nanomed Biotechnol*. 2018;46(8):1935–1947. doi:10.1080/21691401.2017.1396997
3. McLaren JS, White LJ, Cox HC, et al. A biodegradable antibiotic-impregnated scaffold to prevent osteomyelitis in a contaminated in vivo bone defect model. *Eur Cell Mater*. 2014;27:332–349. doi:10.22203/eCM.v027a24
4. Weng W, Nie W, Zhou Q, et al. Controlled release of vancomycin from 3D porous graphene-based composites for dual-purpose treatment of infected bone defects. *RSC Adv*. 2017;7(5):2753–2765. doi:10.1039/C6RA26062D
5. Zhou X, Weng W, Chen B, et al. Mesoporous silica nanoparticles/gelatin porous composite scaffolds with localized and sustained release of vancomycin for treatment of infected bone defects. *J Mater Chem B*. 2018;6(5):740–752. doi:10.1039.C7TB01246B
6. Jiang J, Li L, Li K, et al. Antibacterial nanohydroxyapatite/polyurethane composite scaffolds with silver phosphate particles for bone regeneration. *J Biomater Scie Polym Ed*. 2016;27(16):1584–1598. doi:10.1080/09205063.2016.1221699
7. Pacheco H, Vedantham K, Young A, Marriott I, El-Ghannam A. Tissue engineering scaffold for sequential release of vancomycin and rhBMP2 to treat bone infections. *J Biomed Mater Res A*. 2014;102:4213–4223. doi:10.1002/jbm.a.35092
8. Lu H-T, Lu T-W, Chen C-H, Mi F-L. Development of genipin-crosslinked and fucoidan-adsorbed nano-hydroxyapatite/hydroxypropyl chitosan composite scaffolds for bone tissue engineering. *Int J Biol Macromol*. 2019;128:973–984. doi:10.1016/j.ijbiomac.2019.02.010
9. Oliveira FC, Carvalho JO, Gusmão SBS, et al. High loads of nano-hydroxyapatite/graphene nanoribbon composites guided bone regeneration using an osteoporotic animal model. *Int J Nanomedicine*. 2019;14:865–874. doi:10.2147/IJN.S192456
10. Johnson CT, Garcia AJ. Scaffold-based anti-infection strategies in bone repair. *Ann Biomed Eng*. 2015;43(3):515–528. doi:10.1007/s10439-014-1205-3
11. Flemming H-C, Wingender J. The biofilm matrix. *Nat Rev Microbiol*. 2010;8(9):623–633. doi:10.1038/nrmicro2415
12. Lewis K. Riddle of biofilm resistance. *Antimicrob Agents Chemother*. 2001;45(4):999–1007. doi:10.1128/AAC.45.4.999-1007.2001
13. Magiorakos A-P, Srinivasan A, Carey RB, et al. Multidrug-resistant, extensively drug-resistant and pandrug-resistant bacteria: an international expert proposal for interim standard definitions for acquired resistance. *Clin Microbiol Infect*. 2012;18(3):268–281. doi:10.1111/j.1469-0691.2011.03570.x
14. Shi G, Wang Y, Derakhshanfar S, et al. Biomimicry of oil infused layer on 3D printed poly(dimethylsiloxane): non-fouling, antibacterial and promoting infected wound healing. *Mater Sci Eng C*. 2019;100:915–927. doi:10.1016/j.msec.2019.03.058
15. Guo Z, Xie C, Zhang P, et al. Toxicity and transformation of graphene oxide and reduced graphene oxide in bacteria biofilm. *Scie Total Environ*. 2017;580:1300–1308. doi:10.1016/j.scitotenv.2016.12.093
16. Xu W, Zhang L, Li J, et al. Facile synthesis of silver@graphene oxide nanocomposites and their enhanced antibacterial properties. *J Mater Chem*. 2011;21(12):4593–4597. doi:10.1039/c0jm03376f
17. Pratheesya T, Harish S, Navaneethan M, Sohila S, Ramesh R. Enhanced antibacterial and photocatalytic activities of silver nanoparticles anchored reduced graphene oxide nanostructure. *Mater Res Express*. 2019;6:074003. doi:10.1088/2053-1591/ab1567
18. Kim J, Shin Y, Lee J, et al. The effect of reduced graphene oxide-coated biphasic calcium phosphate bone graft material on osteogenesis. *Int J Mol Sci*. 2017;18(8):1725. doi:10.3390/ijms18081725
19. Zeng X, Mccarthy DT, Deletic A, Zhang X. Silver/reduced graphene oxide hydrogel as novel bactericidal filter for point-of-use water disinfection. *Adv Funct Mater*. 2015;25:4344–4351. doi:10.1002/adfm.201501454
20. Wang H. Antibacterial [2-(methacryloyloxy) ethyl] trimethylammonium chloride functionalized reduced graphene oxide/poly(ethylene-co-vinyl alcohol) multilayer barrier film for food packaging. *R Soc Open Sci*. 2018;66:732–739.
21. Mokkapati V, Pandit S, Kim J, et al. Bacterial response to graphene oxide and reduced graphene oxide integrated in agar plates. *R Soc Open Sci*. 2018;5(11):181083. doi:10.1098/rsos.181083
22. Das DP, Samal A, Das J, Dash A, Gupta H. One-pot fabrication of RGO-Ag3 VO4 Nanocomposites by in situ photoreduction using different sacrificial agents: high selectivity toward catechol synthesis and photodegradation ability. *Photochem Photobiol*. 2014;90:57–65. doi:10.1111/php.12172
23. Deshmukh SP, Patil SM, Mullani SB, Delekar SD. Silver nanoparticles as an effective disinfectant: a review. *Mater Sci Eng C*. 2019;97:954–965. doi:10.1016/j.msec.2018.12.102
24. Huang Y, Song G, Chang X, et al. Nanostructured Ag(+)-substituted fluorhydroxyapatite-TiO(2) coatings for enhanced bactericidal effects and osteoinductivity of Ti for biomedical applications. *Int J Nanomedicine*. 2018;13:2665–2684. doi:10.2147/IJN.S162558
25. Teo WZ, Pumera M. Fate of silver nanoparticles in natural waters; integrative use of conventional and electrochemical analytical techniques. *RSC Adv*. 2014;4(10):5006–5011. doi:10.1039/c3ra43224f
26. Li S, Yu X, Lu R, Liu P, Cai W. Thermal kinetics of self-aggregation and self-assembly of Ag nanoparticles with different capping agents. *J Therm Anal Calorim*. 2015;121(2):855–860. doi:10.1007/s10973-015-4593-1
27. Ko K, Kim MJ, Lee JY, Kim W, Chung H. Effects of graphene oxides and silver-graphene oxides on aquatic microbial activity. *Scie Total Environ*. 2019;651:1087–1095. doi:10.1016/j.scitotenv.2018.09.124
28. Verma P, Maheshwari SK. Applications of silver nanoparticles in diverse sectors. *Int J Nanodimens*. 2019;10:18–36.
29. Zhou Y, Yang J, Cheng X, et al. Electrostatic self-assembly of graphene–silver multilayer films and their transmittance and electronic conductivity. *Carbon*. 2012;50(12):4343–4350. doi:10.1016/j.carbon.2012.04.069
30. Nie W, Peng C, Zhou X, et al. Three-dimensional porous scaffold by self-assembly of reduced graphene oxide and nano-hydroxyapatite composites for bone tissue engineering. *Carbon*. 2017;116:325–337. doi:10.1016/j.carbon.2017.02.013
31. Du S, Shojaei-Zadeh S, Drazer G. Liquid-based stationary phase for deterministic lateral displacement separation in microfluidics. *Soft Matter*. 2017;13(41):7649–7656. doi:10.1039/C7SM01510K
32. Gautam V, Singhal L, Arora SK, Jha C, Ray P. Reliability of Kirby-Bauer disk diffusion method for detecting carbapenem resistance in acinetobacter baumannii-calcoaceticus complex isolates. *Antimicrob Agents Chemother*. 2013;57(4):2003–2004. doi:10.1128/AAC.01450-12

33. Yu X, Liu S, Chen H, et al. CGRP gene-modified rBMSCs show better osteogenic differentiation capacity in vitro. *J Mol Histol*. 2018;49(4):357–367. doi:10.1007/s10735-018-9775-2
34. Tang X-Z, Cao Z, Zhang H-B, Liu J, Yu -Z-Z. Growth of silver nanocrystals on graphene by simultaneous reduction of graphene oxide and silver ions with a rapid and efficient one-step approach. *Chem Commun*. 2011;47(11):3084–3086. doi:10.1039/c0cc05613h
35. Wen Y, Xing F, He S, et al. A graphene-based fluorescent nanoprobe for silver(I) ions detection by using graphene oxide and a silver-specific oligonucleotide. *Chem Commun*. 2010;46(15):2596–2598. doi:10.1039/b924832c
36. Sitko R, Turek E, Zawisza B, et al. Adsorption of divalent metal ions from aqueous solutions using graphene oxide. *Dalton T*. 2013;42(16):5682–5689. doi:10.1039/c3dt33097d
37. Siddiqi KS, Husen A, Rao RAK. A review on biosynthesis of silver nanoparticles and their biocidal properties. *J Nanobiotechnology*. 2018;16:14.
38. Li D, Nie W, Chen L, et al. Self-assembled hydroxyapatite-graphene scaffold for photothermal cancer therapy and bone regeneration. *J Biomed Nanotechnol*. 2018;14(12):2003–2017. doi:10.1166/jbn.2018.2646
39. Stewart PS, Costerton JW. Antibiotic resistance of bacteria in biofilms. *Lancet*. 2001;358(9276):135–138. doi:10.1016/S0140-6736(01)05321-1
40. Kumar P, Nagarajan A, Uchil PD. Analysis of cell viability by the lactate dehydrogenase assay. *Cold Spring Harb Protoc*. 2018;2018:pdb–rot095497.